Dyes and Pigments 184 (2021) 108851

Contents lists available at ScienceDirect

Dyes and Pigments

journal homepage: http://www.elsevier.com/locate/dyepig

Multi-stimuli-responsive fluorescence of axially chiral 4-ene-β-Diketones

Dehua Wu [a,1], Xinyi Fang [b,c,1], Jintong Song [a], Lang Qu [a], Xiangge Zhou [a], Haifeng Xiang [a,*], Jun Wang [b,**], Jin Liu [c,***]

[a] College of Chemistry, Sichuan University, Chengdu, 610041, China
[b] State Key Laboratory of Oral Diseases, Department of Orthodontics, West China Hospital of Stomatology, Sichuan University, Chengdu, 610064, China
[c] Laboratory of Stem Cell Biology, State Key Laboratory of Biotherapy, West China Hospital, Sichuan University, Chengdu, 610064, China

ARTICLE INFO

Keywords:
β-Diketones
Binaphthalene
Excited-state intramolecular proton transfer (ESIPT)
Chiral recognition

ABSTRACT

A unique series of simple, smart, and chiral binaphthalene-substituted 4-ene-β-diketones molecules has been designed and prepared. Their optical properties, charge contribution, and transition process highly depend on their chemical structures. These π-conjugated materials are highly emissive in both solution and solid (emission quantum yield up to 68%), owing to the inhibition of enol-keto tautomerization and the effect of steric hindrance from binaphthalene. Through ethylenic bond hydrolysis, they can be used for not only cation/anion sensing but also chiral amino acids recognition. Moreover, at low concentrations, they have little cytotoxicity to living cells and can stain cytoplasm. Therefore, they afford a new platform in the design of multi-stimuli-responsive, smart, and chiral materials.

1. Introduction

Luminescent (fluorescent or phosphorescent) π-conjugated organic materials [1] have attracted great attention in recent decades owing to their wide applications in organic light-emitting diodes (OLEDs) [2–4], light-emitting electrochemical cells (LECs) [5,6], triplet–triplet annihilation based upconversion [7,8], fluorescence probes [9–11], bio-imaging [12,13], and so forth. In order to tune the emission band (λ_{em}) and quantum yield (Φ) of the organic materials, a number of strategies, including extending π-conjugation, substituent effect, donor-acceptor (DA) system, Förster resonance energy transfer, intramolecular charge transfer (ICT), excimer [2–4,9–11], excited-state intramolecular proton transfer (ESIPT) [14,15], and aggregation-induced emission (AIE) [16–18], are explored. Among them, ESIPT, an intramolecular hydrogen bond between the proton donor (−OH and $-NH_2$) and the proton acceptor (=N− and –C═O) groups in close proximity to each other in a molecule, in particular offers some advantages such as a large Stokes shift with negligible self-absorption and environment-sensitive dual (enol and keto) emissions.

It's well known that β-diketones molecules (Fig. 1(a)) usually exist in a hydrogen-bonded six-membered ring via tautomerization between keto and enol forms [19–21]. However, unlike that of = N−/−OH-based ESIPT molecules [14,15], the tautomerization of β-diketones molecules from planar enol forms into twisted keto forms would destroy the molecular π-conjugated planarity and lead to the emission quenching through the nonradioactive dissipation. Therefore, the simple phenyl--β-diketones (Fig. 1(b)) is non-emissive and some chemical modifications (Fig. 1(c)), such as electron-donating substituent (DA system) [22–25], cyclization [26–31], alkene [26–34], and multiple intramolecular hydrogen bonds [29,31], have been adopted to improve Φ. In addition, β-diketones molecules are widely used as ligands to yield highly emissive B(III) [35–38], Ln(III) [39], Ir(III) [40–42] and Pt(II) [43,44] complexes.

As a class of important axially chiral molecules, 1,1′-binaphthalene-2,2′-diol (BINOL) and 1,1′-binaphthalene-2,2′-diamine (BINAM) recently have become a hot field in optical materials for the applications in chiral recognition [45–49] and circularly polarized luminescence (CPL) [50–54]. However, it is still challenging to prepare highly emissive binaphthalene-based materials, because the binaphthalene group exhibits intramolecular motions through some small-angle rotations around the chiral axis [53,55]. In the present work, combining the

* Corresponding author.
** Corresponding author.
*** Corresponding author.
E-mail addresses: xianghaifeng@scu.edu.cn (H. Xiang), wangjunv@scu.edu.cn (J. Wang), ljamelia@163.com (J. Liu).
[1] These authors contributed equally to this work.

https://doi.org/10.1016/j.dyepig.2020.108851
Received 6 May 2020; Received in revised form 27 July 2020; Accepted 11 September 2020
Available online 28 September 2020
0143-7208/© 2020 Elsevier Ltd. All rights reserved.

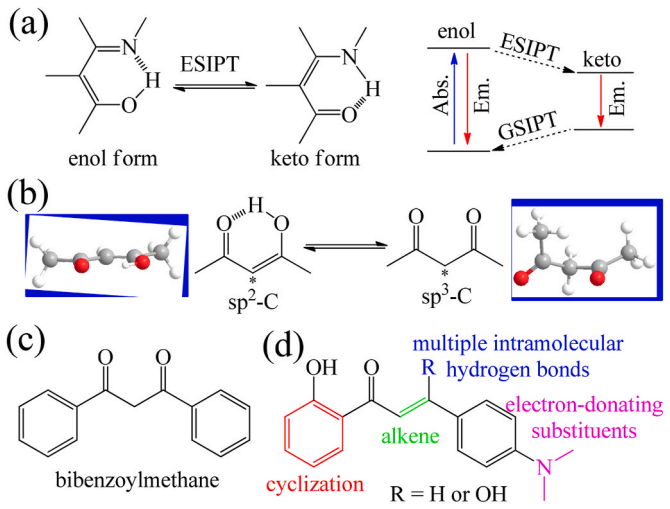

Fig. 1. (a) Enol-keto tautomerization for β-diketones. (b) Chemical structures of non-emissive phenyl-β-diketones and (c) emissive β-diketones molecules.

axially chiral and sterically bulky properties of BINOL, we have linked β-diketones and BINOL by the alkene bridge to achieve chiral luminophors **1–3** (8 pairs of enantiomers, Fig. 2) with large Stokes shifts (up to 6140 cm^{-1}) and high emission quantum yields (up to 68%). The purposes of the presence of alkene linker are: 1) to easily synthesize; 2) to achieve fully π-conjugated molecular system; 3) to inhibit the tautomerization from enol forms into keto forms; 4) to obtain reasonable stability for multi-stimuli-responsive fluorescence through ethylenic bond hydrolysis.

2. Results and discussion

2.1. Synthesis and characterization

All 4-ene-β-diketones molecules were prepared by the modified methods [56,57] with 1,1′-binaphthalene-2,2′-diol-3-carbaldehyde [58] and methyl-β-diketones [59] (Fig. 2). Most of them have a good solubility in organic solvents, such as DMF, DMSO, dichloromethane (DCM), toluene, ethyl acetate (EA) and EtOH, and a bad solubility in cyclohexane and petroleum ether (PE). They don't dissolve in H_2O. Most of them either in solution or in solid state are stable within several months under air. We successfully obtained some good-quality single crystals of (*S*)1–H (yellow particles, CCDC 1963383), (*R*)1-F (yellow particles, CCDC 1963384), and (*S,S*)2 (yellow particles, CCDC 1963385) by the vapor diffusion of DCM/hexane. Based on the ^1H nuclear magnetic resonance (^1H NMR) and x-ray single crystal analysis, 4-ene-β-diketones molecules mainly exist as enol forms in both solution and solid (see the later discussion).

2.2. Photophysical properties

The photophysical properties, including UV/visible absorption and fluorescence data (emission decay lifetime τ and Φ), of all synthesized compounds at room temperature are listed in Tables S1 and S2 (in Supporting Information). The photophysical properties, except circular dichroism (CD), of enantiomers are similar, which are consistent with our previous reports [60–63]. The absorption spectra of all 4-ene-β-diketones molecules in toluene (1.0×10^{-5} mol dm^{-3}) are given in Fig. 3. The presence of weak electron-accepting −Cl and –F substituents [**(*S*)1–F**: λ_{abs} = 377 nm; **(*S*)1–Cl**: λ_{abs} = 386 nm], strong electron-donating −OMe substituent [**(*S*)1–OMe**: λ_{abs} = 380 nm], and π-extended system [**(*S*)-Naph**, λ_{abs} = 387 nm) to the simplest **(*S*)1–H** (λ_{abs} = 380 nm) has little effect on absorption bands. However, strong electron-donating $-NEt_2$ substituent [**(*S*)1–NEt_2**, λ_{abs} = 422 nm] and double binaphthalenes [**(*S,S*)2**, λ_{abs} = 411 nm; **(*S,S*)3**, λ_{abs} = 445 nm] lead to obviously red shifts in absorption spectra.

Density functional theory (DFT) and time-dependent DFT (TD-DFT) were performed by Gaussian 09 program package [B3LYP 6-31G(d,p)] to investigate the UV/visible absorption spectra and charge transfer in excited states. In dilute toluene solution, **(*S*)1–NEt_2** shows a dominating absorption peak (λ_{abs} = 422 nm), which is predicted well by the

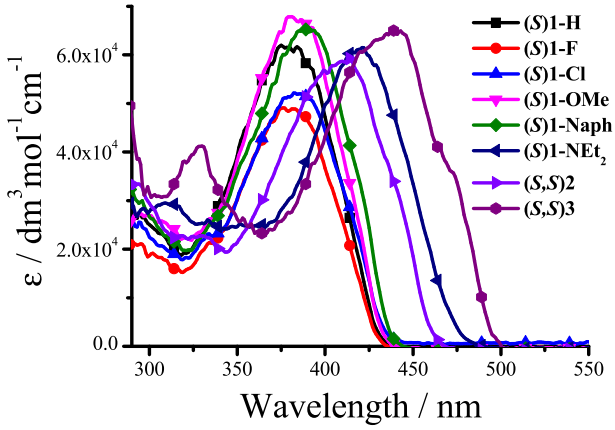

Fig. 3. Absorption spectra in toluene (1.0×10^{-5} mol dm^{-3}).

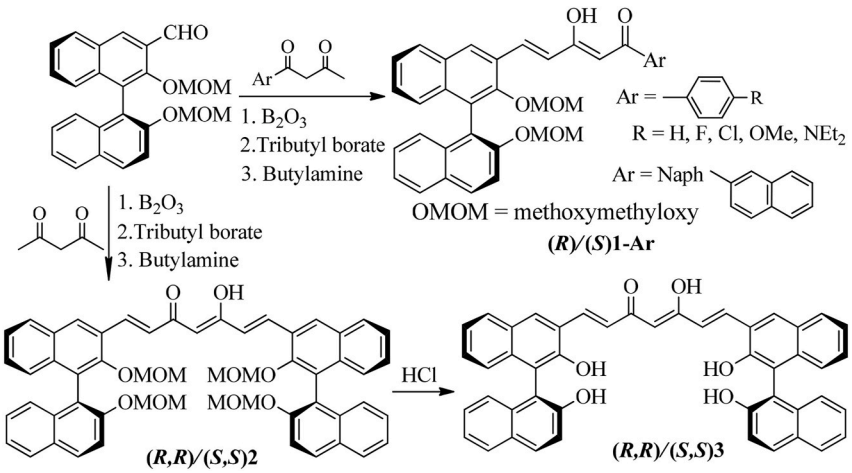

Fig. 2. Synthesis and chemical structures of chiral 4-ene-β-diketones molecules.

theoretical calculation (λ_{abs} = 430 nm) (Fig. 4) and can be contributed to the highest occupied molecular orbital (HOMO) → the lowest unoccupied molecular orbital (LUMO) (excited state 1, 436 nm, 100%, oscillator strength f_{osc} = 1.1415). The energy level diagram and frontier molecular orbitals of **(*S*)1–NEt$_2$** are depicted in Fig. 4 as well. The electron-donating −NEt$_2$ is mostly contributed to the HOMO, whereas the electron-accepting naphthalene ring (the inside naphthalene ring of BINOL) is mostly contributed to the LUMO, clearly indicating the intense ICT from −NEt$_2$ to the inside naphthalene ring [64,65]. Along with this DA charge transfer, the π−π* transition of **(*S*)1–NEt$_2$** is red shifted at 422 nm. It is obvious that the outside naphthalene ring has no contribution to the low-energy transition, because it is almost orthogonal to the π-conjugated molecular plane.

Compared with **(*S*)1–NEt$_2$**, however, **(*S*)1–H** without −NEt$_2$ has a blue-shifted absorption band (λ_{abs} = 380 nm), which can be assigned to HOMO−1 → LUMO (excited state 2, 398 nm, 95%, Fig. 4). The frontier molecular orbitals of **(*S*)1–H** reveal that it has a totally different ICT from the outside naphthalene ring to the other side benzene ring. In addition, the outside naphthalene ring is orthogonal as well, and thus the ICT of **(*S*)1–H** is blue shifted and less efficient (f_{osc} = 0.8908) compared with that of **(*S*)1–NEt$_2$**.

The low-energy absorption band (λ_{abs} = 411 nm) of **(*S,S*)2** is mainly originated from π−π* in HOMO → LUMO (excited state 1, 441 nm, 95%, f_{osc} = 1.2720, Fig. 4). Except the two outside naphthalene rings, the central π-functions of **(*S,S*)2** is efficiently extended into the entire molecule, and consequently **(*S,S*)2** has red-shifted absorption compared with **(*S*)1–H**. Since **(*S,S*)2** is more symmetric than **(*S*)1–NEt$_2$**, little ICT is observed for **(*S,S*)2**. This might be one of factors that **(*S,S*)2** has blue-shifted absorption compared with **(*S*)1–NEt$_2$**, even if **(*S,S*)2** is more conjugated than **(*S*)1–NEt$_2$**.

For the series of **(*S*)1**, only **(*S*)1–NEt$_2$** is highly emissive in non-polar solvent of toluene (λ_{em} = 526 nm, Φ = 58%, τ = 0.55 ns, Tables S1 and S2, and Fig. 5), because **(*S*)1–NEt$_2$** has an efficient DA system. This DA system can be further identified by the obvious solvent effect on emission (Fig. 6). **(*S*)1–NEt$_2$** emits strong blue emission in non-polar solvent of petroleum ether (PE, λ_{em} = 495 nm, Φ = 68%), but its emission becomes orange-yellow along with the emission quenching in the high polar solvent of THF (λ_{em} = 564 nm, Φ = 5.5%). The emission spectrum of **(*S,S*)2** in toluene (λ_{em} = 500 nm, Φ = 17%) is blue-shifted compared with that of **(*S*)1–NEt$_2$**. Moreover, **(*S,S*)2** shows a relatively smaller solvent effect than **(*S*)1–NEt$_2$** (Fig. S1), further identifying that **(*S,S*)2** and **(*S*)1–NEt$_2$** have different transition ways. When the protecting groups of methoxymethyloxy (OMOM) are removed, the resultant **(*S,S*)3** exhibit red-shifted emission at 542 nm with a lower Φ of 5.4% in toluene. In addition, **(*S*)1–NEt$_2$** and **(*S,S*)2** are highly emissive in powder [Φ = 17 and 5.5% for **(*S*)1–NEt$_2$** and **(*S,S*)2**, respectively] and polymethyl methacrylate (PMMA) film [Φ = 48 and 33% for **(*S*)1–NEt$_2$** and **(*S,S*)2**, respectively, Table S1, Fig. 5, and S2].

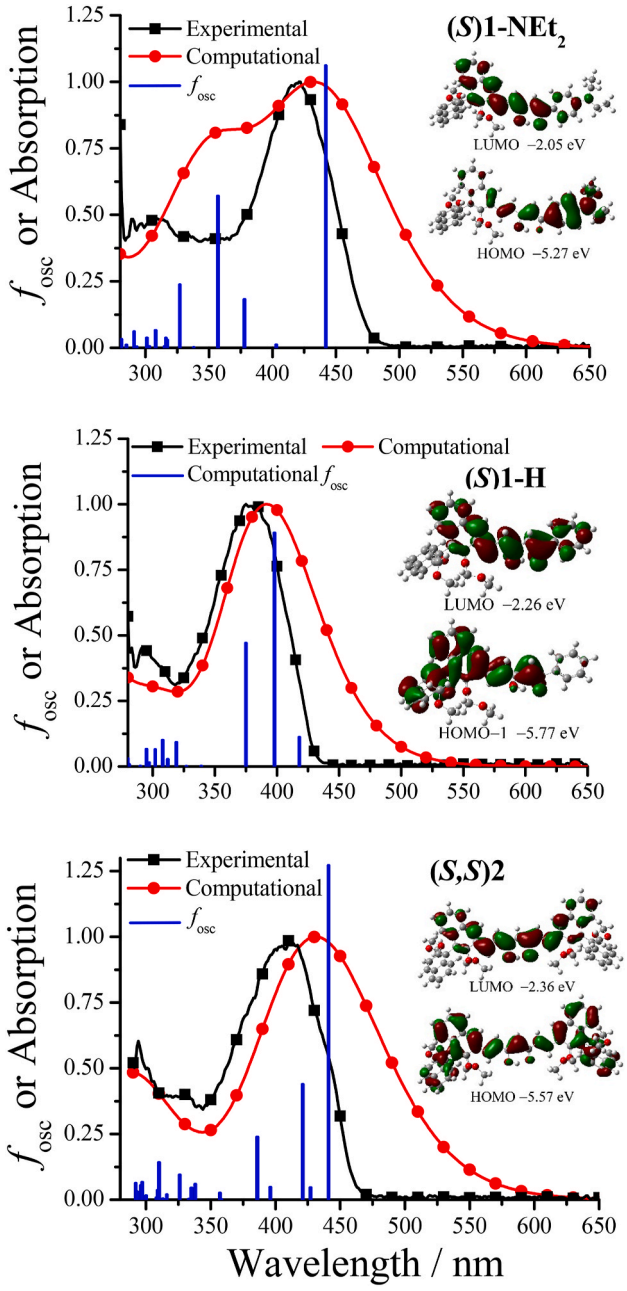

Fig. 4. Computational and experimental absorption spectra (in toluene), energy level diagram, and frontier molecular orbitals of **(*S*)1–NEt$_2$**, **(*S*)1–H**, and **(*S,S*)2**.

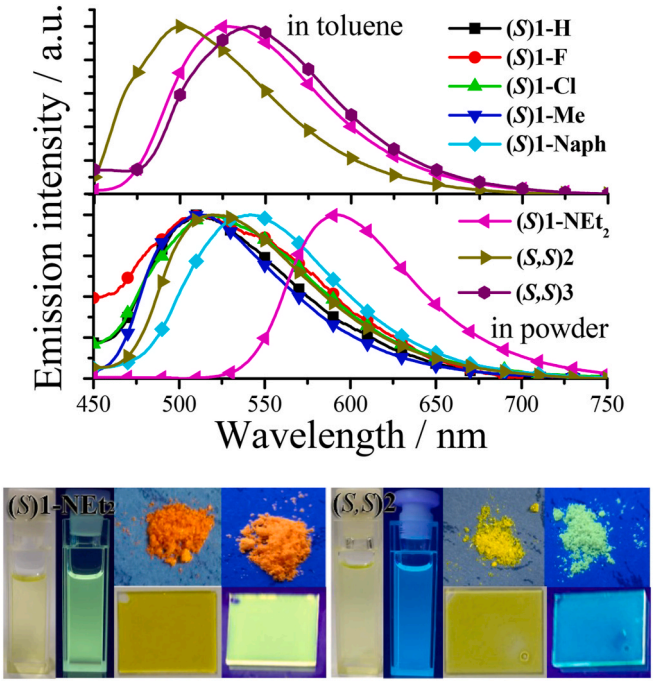

Fig. 5. Normalized emission spectra and photographs (under room and 360 nm UV light) of 4-ene-β-diketones molecules in toluene (1.0×10^{-5} mol dm^{-3}), powder, and PMMA film (1.0 wt%).

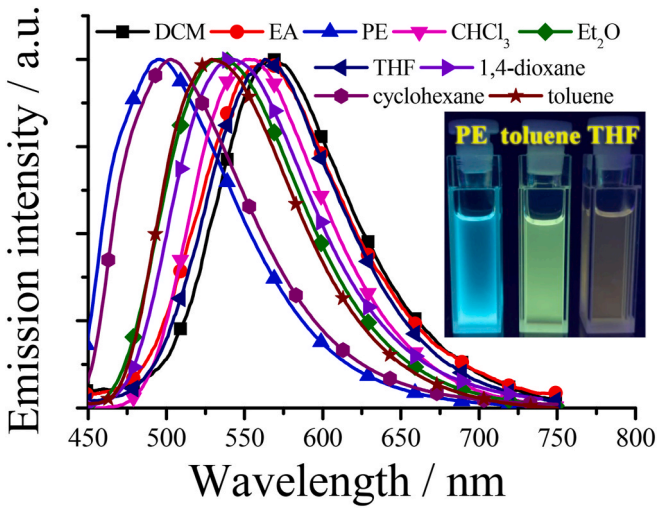

Fig. 6. Normalized emission spectra and photographs (under 360 nm UV light) of **(*S*)1–NEt$_2$** in different solvents (1.0×10^{-5} mol dm^{-3}, excited at 425 nm).

2.3. Hydrolysis in THF solution

All the synthesized solid-state compounds are stable under air. Except **(*S,S*)3**, they are stable in organic solvents. For example, the absorption spectra of **(*S*)1–NEt$_2$** and **(*S,S*)2** in THF exhibit negligible changes (Fig. 7 and S3), but the low-energy absorption band of **(*S,S*)3** in THF decays along with time, resulting in color change from yellow into colorless. Thin-layer chromatography (TLC) analysis reveals that **(*S,S*)3** without protecting groups of OMOM would decompose through ethylenic bond hydrolysis (see the later discussion) [66,67].

2.4. Inhibition of enol-keto tautomerization

β-Diketones molecules are well known to have the tautomerization between keto and enol forms [19–21]. In general, the π-conjugated enol forms are more stable than the keto forms. The enol-keto tautomerization would be influenced by many factors including solvent polarity [68], substitution groups [69,70], pH values, and UV light irradiation [22,71]. However, it should be noted that the enol-keto tautomerization would generally quench emission through the n–π* triplet states of π-diketones [22].

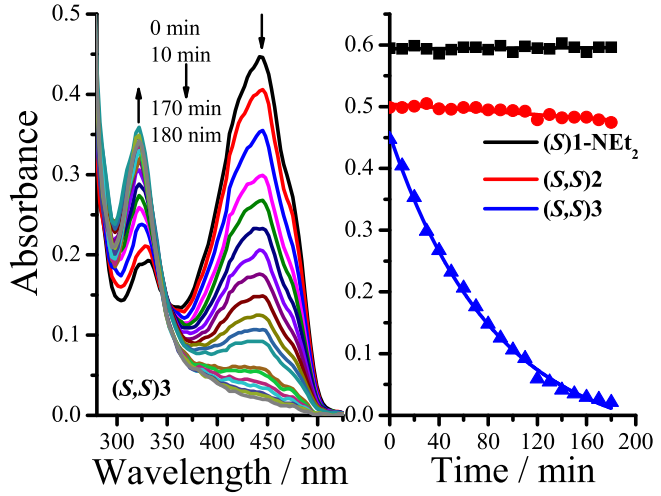

Fig. 7. Absorption spectra of **(*S,S*)3** (left) and absorbance at λ_{abs} of **(*S*)1–NEt$_2$**, **(*S,S*)2** and **(*S,S*)3** (right) in THF at different times (1.0×10^{-5} mol dm^{-3} in THF under room temperature, sunlight and lamplight).

The absorption spectra of **(*S*)1–NEt$_2$** and **(*S,S*)2** have little changes in different organic solvents (Figs. S4 and S5), revealing the absence of solvent-induced enol-keto tautomerization. Based on DFT and TD-DFT calculations (Fig. 8), the keto form of **(*S*)1–NEt$_2$** is much more twisty than enol form, and the former would has obviously blue-shifted absorption (λ_{abs} = 328 nm) compared with the later (λ_{abs} = 430 nm). Indeed, the enthalpy (sum of electronic and thermal enthalpies) and free energy (sum of electronic and thermal free energies) between the enol and keto form of **(*S*)1–NEt$_2$** is 5.81 and 4.37 kcal/mol, respectively. This indicates that the enol-keto tautomerization is endothermic and enol form is thermodynamically more stable than keto form. The absence of solvent-induced enol-keto tautomerization can be further confirmed by the ^{1}H NMR analysis (Fig. 9 and S6). In $CDCl_3$ and DMSO-d_6 solution of **(*S*)1–NEt$_2$**, the ^{1}H NMR peak area of reactive enol-H^1 and ene-H^2 is 0.34 and 0.50, respectively, corresponding to that of H^3 (peak area = 1). Furthermore, there is no ^{1}H NMR signal of keto-H^4 (δ = ~4.0) [72]. Therefore, **(*S*)1–NEt$_2$** mainly exists in the form of enol in both $CDCl_3$ and DMSO-d_6 solution.

At first, the solvent of toluene is used to examine photo-induced enol-keto tautomerization of **(*S*)1–NEt$_2$**. As shown in Fig. S7, the low-energy absorption of **(*S*)1–NEt$_2$** disappears under 360 nm UV irradiation, but it would not be recovered in the darkness. This indicates that the change is not reversible and UV irradiation would promote hydrolysis rather than reversible enol-keto tautomerization. If the solvent is replaced by DMSO, both **(*S*)1–NEt$_2$** and **(*S,S*)2** show a good photostability (Fig. S7).

2.5. X-ray single crystal structures and mechanism of polar solvent-induced fluorescence

The molecule chemical structures and X-ray single-crystal arrangements of organic luminescent materials act an important role in their fluorescence properties. As expected, in solid, **(*S*)1–H**, **(*R*)1-F**, and **(*S,S*)2** exist in the enol form as well (Fig. 10). Two intramolecular = O···HO– hydrogen bonds are found in **(*S*)1–H** (1.735 Å) and **(*R*)1-F** (1.801 Å) single crystal structures and the –OH groups are located in the side of binaphthalene. For more symmetric **(*S,S*)2**, the enol hydrogen is symmetrically positioned between the two oxygen atoms (Fig. S8), and the enol form is stabilized by resonance-assisted hydrogen bonding [73]. Except the outside naphthalene rings and protecting OMOM groups, all the other atoms of **(*S*)1–H**, **(*R*)1-F**, and **(*S,S*)2** are almost located in one plane. The dihedral angle between the two naphthyl rings is 97.2°, 94.2°, and 101.1° for **(*S*)1–H**, **(*R*)1-F**, and **(*S,S*)2**, respectively.

(*S*)1–H and **(*R*)1-F** molecules are cross-stacking, but **(*S,S*)2** molecules are arranged in a Z-type lamellar packing characteristic with a distance of ~7.10 Å (Fig. S9). Owing to the effect of steric hindrance from binaphthalene, there are no intermolecular hydrogen bonds and

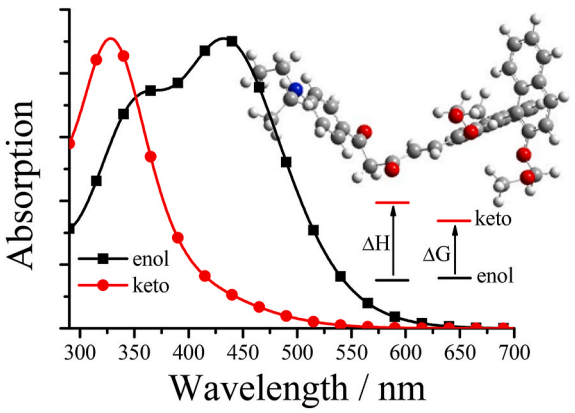

Fig. 8. Computational absorption spectra and enthalpy and free energy levels of the enol and keto form for **(*S*)1–NEt$_2$** and its optimized structure of keto form.

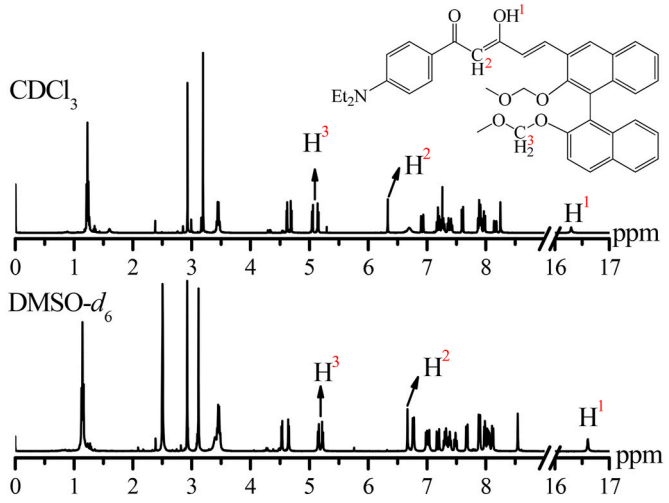

Fig. 9. ^{1}H NMR spectra of **(*S*)1–NEt$_2$** in $CDCl_3$ and DMSO-d_6.

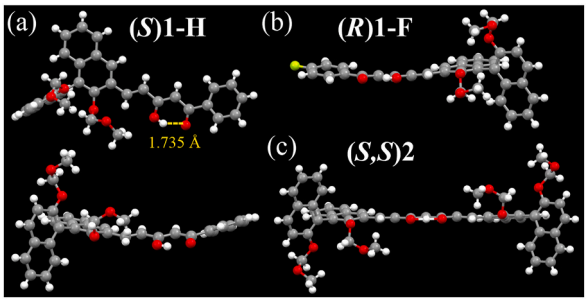

Fig. 10. X-ray single crystal structures of **(*S*)1–H**, **(*R*)1-F**, and **(*S,S*)2**.

π−π interactions in X-ray single crystal structures of **(*S*)1–H**, **(*R*)1-F**, and **(*S,S*)2**. Therefore, both **(*S*)1–H** and **(*R*)1-F** are highly emissive in both solution and solid, combining the fact of inhibition of enol-keto tautomerization.

2.6. Ion probe properties

Since β-diketones in the enol form is acting as an O^O bidentate chelating agent can coordinate with many metal ions [35–44], **(*S*)1–NEt$_2$** (Figs. S10 and S11) and **(*S,S*)2** (Fig. S12−S15) are used as metal ion probes firstly. They have similar sensing performances. As example, the absorption band (λ_{abs} = 412 nm) of **(*S,S*)2** in THF disappears soon (30 min) upon adding Co^{2+} excessively, but other metal ions, such as Ag^+, Al^{3+}, Ca^{2+}, Cu^{2+}, K^+, Li^+, Mg^{2+}, Mn^{2+}, Na^+, Ni^{2+}, Pb^{2+}, and Zn^{2+}, would have much less effect. On the same time, the emission of **(*S,S*)2** (λ_{em} = 501 nm, Φ = 18%) would efficiently be quenched by Co^{2+}. The fluorescence intensity decreases linearly upon the addition of 3–8 equivalents of Co^{2+} and then remains unchanged upon the further addition of Co^{2+} (Fig. S15), indicating that the sensing mechanism is Co^{2+}-promoted hydrolysis but not coordination reaction [74,75]. Of course, we could not rule out the possibility that some other metal ions, such as Cu^{2+} and Ni^{2+}, can coordinate with **(*S,S*)2**, because the addition of these metal ions would result in emission quenching but little changes in absorption spectra (Figs. S12 and S13).

We recently reported that ESIPT salicylaldehyde-based Schiff bases can be used as universal anion hosts/probes through intermolecular hydrogen bonds[[60–63], [76,77] and thus we tried to use **(*S*)1–NEt$_2$** and **(*S,S*)2** (Fig. 11 and S18–S20) as anion probes. As shown in Figs. S16 and S17, upon excessively adding 100 equivalents of anions (Ac^-, Br^-, $C_2O_4^{2-}$, Cl^-, CO_3^{2-}, $H_2PO_4^-$, HCO_3^-, HPO_4^{2-}, HSO_3^-, IO_4^-, NO_2^-, NO_3^-, OH^-, $P_2O_7^{4-}$, PO_4^{3-}, S^{2-}, $S_2O_3^{2-}$, SCN^-, SO_3^{2-}, SO_4^{2-}, $S_2O_8^{2-}$, and I^-) to the THF solution of **(*S*)1–NEt$_2$** (λ_{abs} = 422 nm, λ_{em} = 564 nm, Φ = 5.5%), only I^- dramatically brings down absorption and emission intensity. For **(*S,S*)2**, however, I^-, Br^-, NO_2^-, SCN^-, and S^{2-} would obviously decrease the absorption and emission intensity (Fig. 11). I^- was used to perform the working curve (Fig. S18). The emission intensity (λ_{em} = 501 nm) of **(*S,S*)2** linearly reduces (correlation coefficient R^2 = 0.978, n = 15) along with 0.2–1.6 equivalents of I^-.

TLC analysis (Fig. S19) reveals that **(*S,S*)2** would decompose to yield the starting materials of BINOL-based formaldehyde and methyl-β-diketones (Fig. 2) through ethylenic bond hydrolysis [66,67]. The dynamics of the hydrolysis reaction is studied by time-dependent absorption and fluorescence (Fig. 11) spectra. The I^--promoted hydrolysis is very fast and needs about 20 min to reach equilibrium at room temperature.

2.7. Chirality and chiral recognition

The chirality properties of **(*R*)/(*S*)1–NEt$_2$** and **(*R,R*)/(*S,S*)2** are investigated by CD spectra (Fig. 12). Even in dilute MeCN, the CD signals of **(*R*)/(*S*)1–NEt$_2$** and **(*R,R*)/(*S,S*)2** are still strong. **(*S*)1–NEt$_2$** and **(*S,S*)2**, the (*S*) enantiomers, show positive Cotton peak at ~340 nm and negative Cotton peaks at ~270 and ~330 nm. **(*R*)1-NEt$_2$** and **(*R,R*)2**, the (*R*) enantiomers, exhibit exactly the mirrored CD spectra, indicating that they are two pairs of enantiomers. Combining with previous work [45–49] these CD signals in shorter wavelength regions (<350 nm) are mainly originated from chiral binaphthalene itself. It is strange that the Cotton peaks in longer wavelength regions (>350 nm) are relatively weak, even although they have strong absorption at 405–426 nm in MeCN (Table S2) [78,79]. This might be caused by the fact that the absorption at longer wavelength regions is mainly originated from the central π-conjugations and the outside naphthalene rings (axial chirality) have little contribution to the absorption at longer wavelength regions (Fig. 4).

Chiral **(*S*)1–NEt$_2$** and **(*S,S*)2** might be used for the chiral recognition of amino acids through intermolecular hydrogen bonds [45–49] or hydrolysis. When adding 19 pairs of chiral L-/D-amino acids and a achiral amino acid of Gly to the **(*S*)1–NEt$_2$** THF solution, the intensity of absorption and emission peak shows little changes (Figs. S20 and S21), revealing that **(*S*)1–NEt$_2$** can't be hydrolyzed by amino acids and has no ability to probe amino acids. On the other hand, the absorption and emission of **(*S,S*)2** can be decreased obviously by many amino acids, especially by D-Lys, L-Pro, L-Lys, D-Tyr, and D-Pro (Fig. 13).

Interestedly, **(*S,S*)2** has the ability of chiral recognition for L-/D-Tyr (Fig. 14). The selective recognition of chiral molecular enantiomers is related to the enantiomeric emission difference ratio, *ef*, according to $ef = (I_L - I_0)/(I_D - I_0)$, in which I_0 represents the emission intensity of receptor in the absence of a chiral substrate and I_L and I_D are the emission intensities in the presence of L- and D-substrates, respectively. The *ef* of L- and D-Tyr is up to 1.81 (Fig. S22) for **(*S,S*)2**. The Tyr-promoted hydrolysis of **(*S,S*)2** is relatively slow and needs about 24 and 10 h to reach equilibrium at room temperature and 50 °C, respectively (Fig. S23).

2.8. Living cell imaging

Fluorescent dyes are promising tools for turn-on, real-time, onsite and non-invasive visualization of biological molecules and processes in live cells and organisms. Since **(*R*)/(*S*)1–NEt$_2$** have large Stokes shifts (Table S2) and high resistance to photobleaching, anions and amino acids, they are used for cell imaging. The metabolic viability of human colon cancer cells (SW480) is determined through Cell Counting Kit-8 (CCK-8) assay to evaluate the cytotoxicity of **(*R*)/(*S*)1–NEt$_2$**. **(*R*)/(*S*)1–NEt$_2$** with big π-conjugated system would have high cytotoxicity to kill the cells if their concentrations are higher than 1.0×10^{-5} mol dm^{-3} (Fig. S24). However, if their concentrations are lower than 1.0×10^{-6} mol dm^{-3}, **(*R*)/(*S*)1–NEt$_2$** would have low cytotoxicity and promote cell growth (Fig. S25).

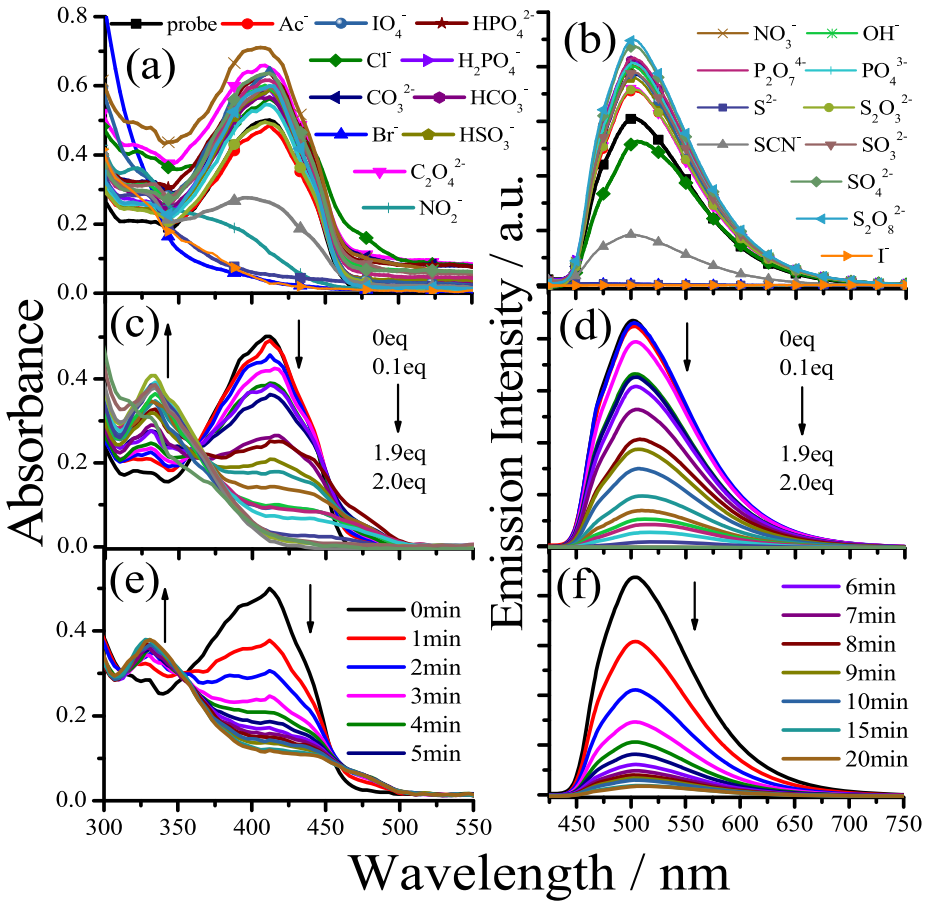

Fig. 11. Absorption and emission spectra of **(*S,S*)2** (1.0×10^{-5} mol dm^{-3} in THF, excited at 400 nm) upon adding 100 equivalents of different anions (a and b) or different equivalents of I−(c and d). Reaction dynamics of (e) absorption and (f) emission spectra after adding 1.5 equivalents of I^-.

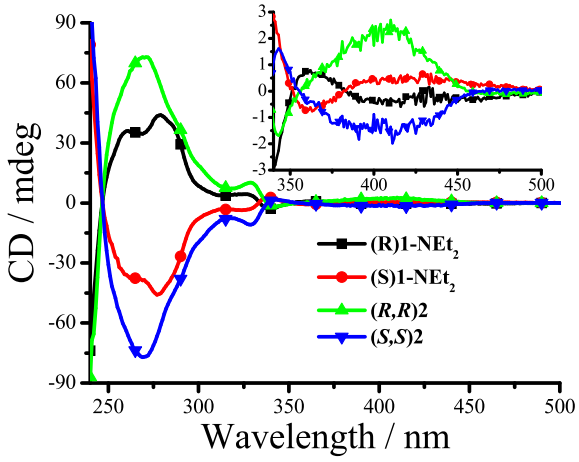

Fig. 12. CD spectra of **(*R*)/(*S*)1–NEt$_2$** and **(*R,R*)/(*S,S*)2** in MeCN (5.0×10^{-5} mol dm^{-3}).

The SW480 cells have negligible background fluorescence without staining the dye. If the cells are incubated with **(*R*)/(*S*)1–NEt$_2$**, however, intense intracellular green emission is observed (Fig. 15). The cell imaging also demonstrates that **(*R*)/(*S*)1–NEt$_2$** at a low concentration have little impact on the growth of living cells. Co-staining **(*R*)/(*S*)1–NEt$_2$** with a commercial cell nucleus dye of 4′6-diamidino-2-phenylindole (DAPI) are carried out further to reveal the location of the dye in the living cells. When excited by 400 nm, the co-stained cells give strong blue emission mainly from DAPI. On the other hand, when excited 480 nm, the strong green emission mainly from **(*R*)/(*S*)1–NEt$_2$** are observed. The merge photos reveal that **(*R*)/(*S*)1–NEt$_2$** are located in cytoplasm rather than cell nucleus. In addition, **(*R*)/(*S*)1–NEt$_2$** are one pair of enantiomers, but they have the similar the staining locations in the cells.

3. Conclusions

In summary, we have prepared and reported a unique series of alkene-linked BINOL-β-diketones molecules. The x-ray single crystal structures and TD-DFT calculations reveal that small changes in chemical structures would lead to big differences in charge distribution and transition process. Since the presence of alkene linker and BINOL would help to prevent from enol-keto tautomerization and intermolecular π−π interactions, respectively, these π-conjugated materials are highly emissive in both solution and solid. Through alkene hydrolysis, they can be used for not only cation/anion sensing but also chiral amino acids recognizing. Moreover, at low concentrations, these fluorescent dyes with little cytotoxicity to living cells can stain and light up cytoplasm. Therefore, we believe that they potentially provide a new and simple way to design multi-stimuli-responsive, smart, and chiral materials. Further studies on CPL applications are currently underway in our laboratory.

4. Experimental section

4.1. Materials and instrumentation

All reagents were purchased from commercial suppliers and used without further purification. ^{1}H NMR (400 MHz) spectra were recorded in DMSO-d_6. Chemical shifts are reported in ppm using

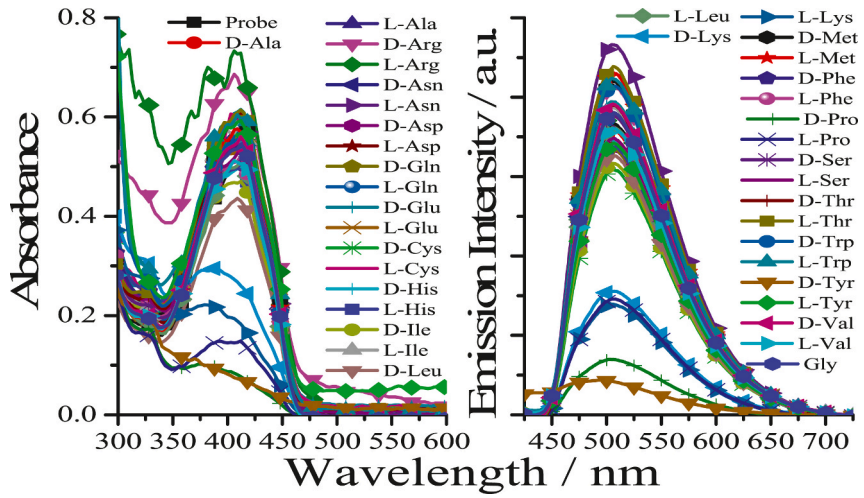

Fig. 13. Absorption and emission spectra of ***(S,S)*2** in THF (1.0×10^{-5} mol dm^{-3}, excited at 400 nm) upon adding different 100 equivalents of amino acids.

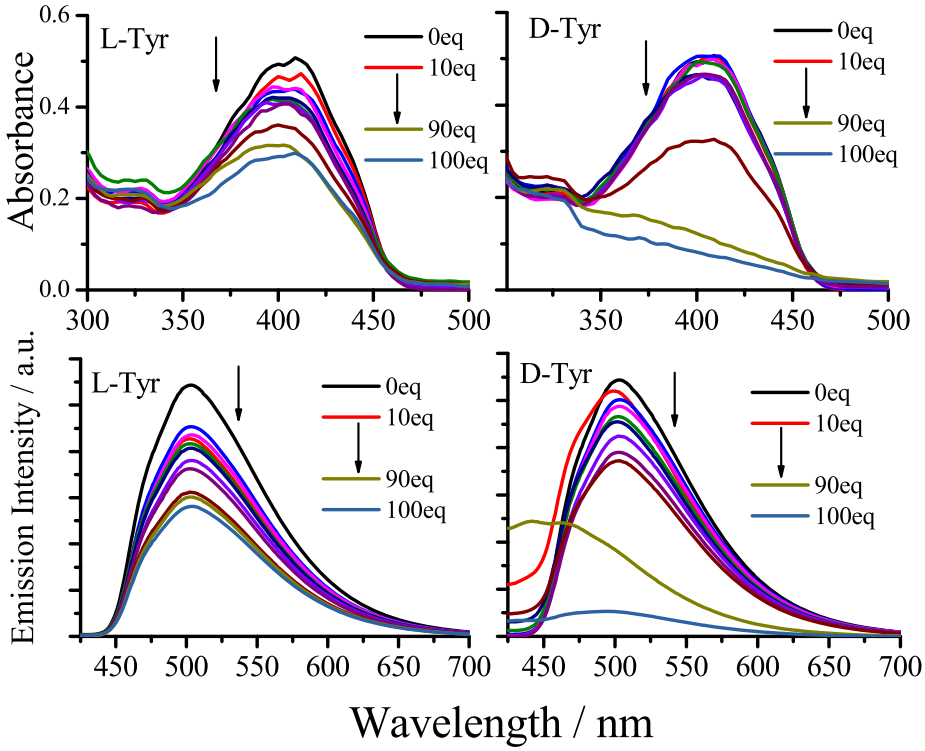

Fig. 14. Absorption and emission spectra of ***(S,S)*2** in THF (1.0×10^{-5} mol dm^{-3}, excited at 400 nm) upon adding different equivalents of L-/D-Tyr.

tetramethylsilane as internal standard. UV/vis absorption spectra were recorded using a U5100 (Hitachi) spectrophotometer with quartz cuvettes of 1 and 0.1 cm pathlength for solution and PMMA film, respectively. Fluorescence spectra were obtained using F-7000 Fluorescence spectrophotometer (Hitachi) at room temperature. The slit width was 5 nm and 2.5 nm for excitation and emission. The photon multiplier voltage was 400 V. Emission decay lifetime was determined by Hamamatsu FL920S instrument. CD spectra were recorded using a Chirascan plus qCD (Applied Photophysics) at room temperature. HR-MS were obtained with a Waters-Q-TOF-Premier (electrospray ionization mass spectrometry, ESI).

4.2. Measurement of fluorescence quantum yield (Φ)

The quantum yield of a solution sample was measured by the optical dilute method with a standard of quinine sulfate ($\Phi_r = 0.55$, quinine in 0.05 mol dm^{-3} sulfuric acid) calculated by: $\Phi_s = \Phi_r(B_r/B_s)(n_s/n_r)^2(D_s/D_r)$, where the subscripts s and r refer to the sample and reference standard solution respectively; n is the refractive index of the solvents; D is the integrated intensity. The excitation intensity B is calculated by: $B = 1–10^{-AL}$, where A is the absorbance at the excitation wavelength and L is the optical path length (L = 1 cm in all cases). The refractive indices of the solvents at room temperature are taken from standard source. The quantum yield of a solid sample was measured by an integrating sphere.

4.3. X-ray crystallographic analysis

The determination of the unit cell and data collection for four single crystal samples were performed on a Xcalibur E X-ray single crystal diffractometer equipped with graphite monochromator Mo Kα (λ =

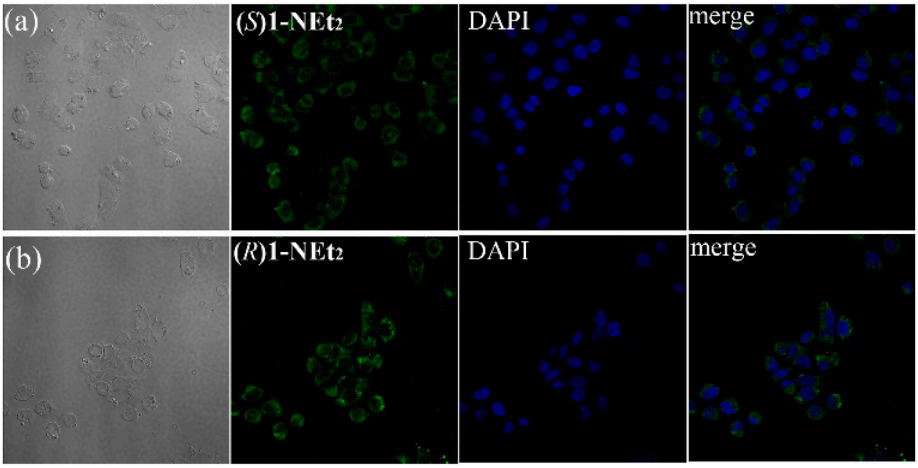

Fig. 15. Brightfield and fluorescence images of SW480 cells co-stained with DAPI and (a) **(*S*)1–NEt_2** and (b) **(*R*)1-NEt_2** excited at 380 and 460 nm for DAPI and **(*R*)/(*S*)1–NEt_2**, respectively.

0.71073 Å) radiation. The data collection was executed using CrysAlisPro program. Structures were solved by direct method and successive Fourier difference syntheses (SHELXS-97), and were refined by full matrix least-squares procedure on F2 with anisotropic thermal parameters for all nonhydrogen atoms (SHELXL-97).

4.4. Computational details

Calculations were carried out using the Gaussian 09 software package [B3LYP 6-31G(d,p)] based on the X-ray single-crystal structure or its modified structures. The ground state geometry was optimized using DFT. The excited states were predicted using the ground state geometry using TD-DFT, from where UV/Vis absorption (pcm method for solvent effect; 100 excited states) were predicted.

4.5. Cell culture methods and imaging

The imaging of SW480 cells was finished by Fluorescence Vertical Microscope-Zeiss AX10 imager A2/AX10 cam HRC. The human gastric cancer cell lines (IM95 m), purchased from JCRB Cell Bank (NIBIO, Osaka, Japan), was cultured in Modified PRMI Medium (Hyclone, Utah, USA) supplemented with 10% fetal bovine serum (Gibco, California, USA), 100 U/ml penicillin and 100 μg/ml streptomycin (Hyclone, Utah, USA) at 37 °C in an atmosphere containing 5.0% CO_2. Cells were routinely grown in 100-mm plastic tissue culture dishes (Corning, New York, USA) and harvested using a 0.25% Trypsin-EDTA solution (Corning, New York, USA) when they reached the logarithmic growth phase. Cells were maintained in these culture conditions for all experiments. After removing the incubating media and rinse with PBS for three times, the cells were incubated with the dye (the dye prepared by diluting DMSO with PBS to the appropriate concentration of 1.0×10^{-6} mol dm^{-3}) in PBS for 2 h at room temperature. Then, the cells were washed three times with PBS and incubated with aqueous alkali for 15 min. At last, the cells were imaged with confocal microscope.

4.6. Cytotoxicity studies

To evaluate the toxicity of the fluorescent dyes, Cell Counting Kit-8 (CCK-8 assay, Sigma, St. Louis, MO, USA) was used to assess the living cells viability. The more toxic the fluorescent dyes are, the less viability the cells have. Modified PRMI media with different concentrations of the dye were added into each well, after the cells are seeded at a density of 2000 per well in the 96-well plate. Thereafter, the CCK-8 assay was used on 2 h and the OD value was measured by BioTek ELX800 (Bio-Tek, Winooski, VT, USA) at the wavelength of 450 nm.

4.7. Measurement of ion probes

Anion titration experiment was started with the dye (10 mL) of known concentration (1.0×10^{-5} mol dm^{-3} in THF). For the titration, various metal ions (1.0–0.10 mol dm^{-3} NO_3^- or Cl^- salts in water) and anions (1.0–0.10 mol dm^{-3} sodium or potassium salts in water) were added by a microsyringe. All types of absorption and fluorescence measurement were monitored at about 1 h after the addition of the ion to the dye solution at room temperature.

4.8. Measurement of amino acid probes

Amino acid titration experiment was started with the dye (10 mL) of known concentration (1.0×10^{-5} mol dm^{-3} in THF). For the titration, various *D*- or L-amino acids (1.0×10^{-2}–1.0×10^{-1} mol dm^{-3} in water) were added by a microsyringe. All types of absorption and fluorescence measurement were monitored at about 24 h after the addition of the amino acids to the dye solution at room temperature.

4.8.1. Synthesis of (R)/(S)-3-formyl-2,2′-bis(methoxymethyloxy)-1,1′-binaphthalene [58]

1.3 M t-BuLi in pentane (45 mL, 58.5 mmol) was added dropwisely to 300 mL dry THF solution of (*S*)/(*R*)-2,2′-bis(methoxymethyloxy)-1,1′-binaphthalene (10 g, 26.7 mmol) at −78 °C. After stirring for 1 h, DMF (2.8 mL, 36.4 mmol) was added dropwisely, after 1.5 h, additional DMF (1 mL, 12.9 mmol) was added to the reaction mixture. The mixture was allowed to warm to room temperature slowly, quenched with saturated NH_4Cl after stirring for 9 h (total reaction time), and extracted with EtOAc. The combined extracts were washed with water and brine, and dried over Na_2SO_4. The solvent was removed under reduced pressure at room temperature. Purification by column chromatography on silica gel (PE/EtOAc = 20/1) gave the product in 56% yield (6 g) as a yellow solid. 20% (2 g) of the starting material was also recovered.

4.8.2. General synthesis of 1-aryl-1,3-butadione [59]

To a suspension of NaH (1.60 g of dispersion in oil, 40 mmol) in EtOAc (20 mL) was added a solution of 1-arylethanone (10 mmol) in EtOAc (20 mL) slowly at 0 °C, and then, the mixture was stirred at room temperature for 12 h. The mixture was carefully treated with 10% aqueous NH_4Cl (30 mL) and adjusted to pH 5 with hydrochloric acid. The aqueous phase was separated and extracted with EtOAc. The combined organic extracts were dried over anhydrous Na_2SO_4 and concentrated under reduced pressure. Purification by column chromatography on silica gel (PE/EtOAc) gave the desired 1-Aryl-1,3-butadione (keto-−enol mixture).

4.8.3. General synthesis of (R)/(S)1 and (R,R)/(S,S)2 [56]

In a 100 mL round bottom flask, an acetylacetone derivative (5 mmol, 5 eq.) was dissolved in 15 mL of ethyl acetate. Boron oxide (174 mg, 2.5 mmol, 2.5 eq.) was added and the solution was stirred for 30 min at 60 °C. Then, 20 mL of an ethyl acetate solution of the appropriate (*R*)/(*S*)-3-formyl-2,2′-bis(methoxymethyloxy)-1,1′-binaphthalene (1 mmol, 1 eq.) with the tributylborate (1.15 g, 5 mmol, 5 eq.) was added and the solution was further stirred for 30 min at this temperature. Finally, butylamine (73 mg, 1 mmol, 1 eq.) was added dropwise. The reaction was heated at reflux for 14 h. After cooling to 60 °C, 30 mL of 0.4 M HCl was added and the mixture was stirred for 30 min at 60 °C. After cooling, the aqueous phase was separated and extracted with EtOAc. The combined organic extracts were dried over anhydrous $MgSO_4$ and concentrated under reduced pressure. Purification by column chromatography on silica gel (PE/EtOAc) gave the desired product.

4.8.4. General synthesis of (R,R)/(S,S)3 [57]

To an ice-cooled solution of (*R,R*)/(*S,S*)2 (0.87 g, 1.0 mmol) in EtOH (20 mL) was added HCl (12 N, 15 mL), and the resulting mixture was stirred at 0 °C for 3 h, and then extracted with diethyl ether (3 × 50 mL). The combined organic extracts were washed with brine, dried over $MgSO_4$, and evaporated under reduced pressure. The residue was then dried in vacuum to afford 0.65 g of (*R,R*)/(*S,S*)3 as an orange-yellow solid. Yield: 95%

(*R*)/(*S*)1–H (Yield: 52%): δ_H (400 MHz, DMSO-d_6) 16.26 (1H, s), 8.58 (1H, s), 8.19–8.03 (5H, m), 7.98 (1H, d, *J* = 8.0), 7.71–7.63 (2H, m), 7.58 (2H, t, *J* = 7.5), 7.52–7.46 (1H, m), 7.41–7.23 (4H, m), 7.02 (2H, dd, *J* = 16.7, 8.5), 6.89 (1H, s), 5.18 (2H, dd, *J* = 30.1, 6.9), 4.60 (2H, dd, *J* = 48.7, 5.7), 3.11 (3H, s), 2.94 (3H, s). δ_C (101 MHz, DMSO-d_6) 189.75, 179.31, 152.89, 152.03, 136.04, 135.59, 134.57, 133.64, 133.62, 130.94, 130.51, 130.41, 129.50, 129.44, 129.26, 129.20, 128.55, 128.26, 128.25, 128.04, 127.85, 127.29, 126.36, 126.21, 125.60, 125.55, 125.04, 124.46, 119.10, 116.39, 99.47, 98.62, 94.36, 56.96, 55.95. HRMS (ESI): Calculated for $C_{35}H_{30}O_6$ [[M+Na]$^+$] 569.1940, found 569.1929.

(*R*)/(*S*)1–F (Yield: 60%): δ_H (400 MHz, DMSO-d_6) 16.18 (1H, s), 8.58 (1H, s), 8.16 (5H, m), 8.07 (1H, d, *J* = 8.1), 7.99 (1H, d, *J* = 8.1), 7.70 (1H, d, *J* = 9.2), 7.49 (1H, t, *J* = 7.4), 7.41 (5H, m), 7.05 (2H, dd, *J* = 15.7, 8.5), 6.89 (1H, s), 5.20 (2H, dd, *J* = 29.9, 6.9), 4.62 (2H, dd, *J* = 48.5, 5.7), 3.13 (3H, s), 2.95 (3H, s). δ_C (101 MHz, DMSO-d_6) 188.88, 178.79, 166.78, 164.27, 152.90, 152.03, 135.59, 134.58, 133.63, 132.77, 130.94, 130.81, 130.72, 130.50, 129.51, 129.25, 129.20, 128.54, 128.26, 128.02, 127.26, 126.38, 126.18, 125.60, 125.37, 125.05, 124.45, 119.12, 116.59, 116.38, 99.47, 98.47, 94.37, 56.93, 55.93. HRMS (ESI): Calculated for $C_{35}H_{29}FO_6$ [[M+Na]$^+$] 587.1846, found 587.1833.

(*R*)/(*S*)1–Cl (Yield: 56%): δ_H (400 MHz, DMSO-d_6) 16.13 (1H, s), 8.56 (1H, s), 8.09 (5H, m), 7.97 (1H, d, *J* = 8.0), 7.66 (3H, m), 7.47 (1H, dd, *J* = 11.1, 4.0), 7.31 (4H, m), 7.02 (2H, dd, *J* = 16.9, 8.5), 6.89 (1H, s), 5.18 (2H, dd, *J* = 30.2, 6.9), 4.59 (2H, dd, *J* = 48.8, 5.7), 3.10 (3H, s), 2.93 (3H, s). δ_C (101 MHz, DMSO-d_6) 188.45, 179.47, 152.90, 152.04, 138.49, 135.91, 134.82, 134.61, 133.63, 130.93, 130.51, 129.60, 129.53, 129.51, 129.21, 128.73, 128.44, 128.05, 127.26, 126.29, 125.62, 125.50, 125.05, 124.45, 119.11, 116.39, 99.47, 98.60, 94.38, 60.22, 60.22, 56.94, 55.94, 55.37, 55.37. HRMS (ESI): Calculated for $C_{35}H_{29}ClO_6$ [[M+Na]$^+$] 603.1550, found 603.1549.

(*R*)/(*S*)1–OMe (Yield: 76%): δ_H (400 MHz, DMSO-d_6) 16.39 (1H, s), 8.58 (1H, s), 8.12 (5H, m), 7.99 (1H, d, *J* = 8.1), 7.71 (1H, d, *J* = 9.2), 7.48 (1H, dd, *J* = 11.1, 4.0), 7.32 (4H, m), 7.08 (4H, m), 6.84 (1H, s), 5.21 (2H, dd, *J* = 29.7, 6.9), 4.64 (2H, dd, *J* = 48.3, 5.7), 3.86 (3H, s), 3.14 (3H, s), 2.96 (3H, s). δ_C (101 MHz, DMSO-d_6) 189.73, 177.62, 163.81, 152.92, 152.02, 134.71, 134.50, 133.67, 131.41, 130.98, 130.48, 130.19, 129.52, 129.35, 129.21, 128.71, 128.53, 128.05, 127.89, 127.24, 126.36, 126.13, 125.60, 125.09, 124.44, 119.20, 116.40, 114.71, 114.62, 99.46, 98.20, 94.39, 56.92, 56.82, 55.98, 55.93. HRMS (ESI): Calculated for $C_{36}H_{32}O_7$ [[M+Na]$^+$] 599.2046, found 599.2044.

(*R*)/(*S*)1-Naph (Yield: 60%): δ_H (400 MHz, DMSO-d_6) 16.29 (1H, s), 8.68 (2H, d, *J* = 61.8), 8.08 (8H, m), 7.67 (3H, m), 7.50 (1H, t, *J* = 7.4), 7.34 (4H, m), 7.03 (3H, dd, *J* = 16.0, 8.8), 5.19 (2H, dd, *J* = 30.5, 6.9), 4.61 (2H, dd, *J* = 49.0, 5.7), 3.12 (3H, s), 2.95 (3H, s). δ_C (101 MHz, DMSO-d_6) 189.58, 179.18, 152.92, 152.08, 135.60, 135.53, 134.60, 133.66, 133.43, 132.80, 130.98, 130.51, 129.97, 129.52, 129.34, 129.26, 129.04, 128.55, 128.31, 128.19, 128.01, 127.55, 127.49, 127.27, 126.45, 126.41, 126.18, 125.62, 125.08, 124.45, 123.72, 119.16, 116.40, 99.50, 99.01, 94.38, 56.96, 55.95, 55.37. HRMS (ESI): Calculated for $C_{39}H_{32}O_6$ [[M+Na]$^+$] 619.2097, found 619.2091.

(*R*)/(*S*)1–NEt$_2$ (Yield: 62%): δ H (400 MHz, DMSO-d_6) 16.60 (1H, s), 8.54 (1H, s), 8.05 (2H, dd, J = 9.6, 5.1), 7.98 (2H, m), 7.89 (2H, d, J = 9.0), 7.68 (1H, d, J = 9.2), 7.48 (1H, t, J = 7.5), 7.34 (3H, ddd, J = 15.7, 11.7, 7.3), 7.19 (1H, d, J = 16.0), 7.01 (2H, dd, J = 14.2, 8.5), 6.77 (2H, d, J = 9.1), 6.67 (1H, s), 5.22 (1H, d, J = 6.9), 5.15 (1H, d, J = 7.0), 4.65 (1H, d, J = 5.6), 4.53 (1H, d, J = 5.6), 3.46 (4H, dd, J = 14.0, 7.0), 3.12 (3H, s), 2.92 (3H, s), 1.14 (6H, t, J = 7.0). δ_C (101 MHz, DMSO-d_6) 189.23, 175.35, 152.63, 151.66, 151.45, 134.05, 133.39, 132.89, 131.74, 130.77, 130.74, 130.25, 130.18, 129.29, 129.24, 129.21, 128.88, 128.29, 127.52, 127.43, 127.02, 126.00, 125.87, 125.77, 125.32, 124.81, 124.20, 123.58, 121.91, 118.93, 116.14, 110.82, 99.12, 97.60, 94.09, 56.67, 55.69, 44.15, 12.63. HRMS (ESI): Calculated for $C_{39}H_{39}NO_6$ [[M+Na]$^+$] 640.2675, found 640.2672.

(*R,R*)/(*S,S*)2 (Yield: 75%): δ_H (400 MHz, DMSO-d_6) 16.18 (1H, s), 8.65 (2H, s), 8.12 (6H, m), 7.99 (2H, d, *J* = 8.1), 7.68 (2H, d, *J* = 9.2), 7.50 (2H, t, *J* = 7.4), 7.35 (8H, ddd, *J* = 22.8, 14.8, 6.4), 7.02 (4H, dd, *J* = 17.5, 8.5), 6.33 (1H, s), 5.19 (4H, dd, *J* = 27.4, 6.9), 4.60 (4H, dd, *J* = 47.2, 5.7), 3.12 (6H, s), 2.95 (6H, s). δ_C (101 MHz, DMSO-d_6) 183.73, 152.89, 152.05, 136.36, 134.65, 133.61, 130.93, 130.52, 129.50, 129.30, 129.04, 128.56, 128.48, 128.11, 127.31, 126.30, 126.20, 125.59, 125.03, 124.48, 119.08, 116.40, 102.84, 99.46, 94.36, 65.39, 56.99, 55.95. HRMS (ESI): Calculated for $C_{55}H_{48}O_{10}$ [[M+Na]$^+$] 891.3145, found 891.3112.

(*R,R*)/(*S,S*)3 (Yield: 95%): δ_H (400 MHz, DMSO-d_6) 16.79 (1H, s), 9.47 (2H, s), 8.83 (2H, s), 8.52 (2H, s), 8.27 (2H, t, *J* = 10.3), 7.94 (8H, m), 7.29 (11H, m), 6.93 (2H, d, *J* = 8.3), 6.83 (2H, m). δ_C (101 MHz, DMSO-d_6) 180.77, 154.57, 152.20, 141.05, 135.68, 134.72, 130.51, 130.20, 129.44, 128.86, 128.63, 128.56, 128.13, 126.74, 124.89, 124.86, 124.34, 123.90, 122.92, 120.83, 119.30, 117.53, 113.36, 108.16. HRMS (ESI): Calculated for $C_{47}H_{32}O_6$ [[M+Na]$^+$] 715.2097, found 715.2087.

CRediT authorship contribution statement

Dehua Wu: Investigation, Formal analysis, Writing - original draft. **Xinyi Fang:** Cell imaging. **Jintong Song:** Conceptualization, Methodology. **Lang Qu:** computation. **Xiangge Zhou:** Methodology. **Haifeng Xiang:** Resources, Supervision, Writing. **Jun Wang:** Resources, Supervision. **Jin Liu:** Resources, Supervision.

Declaration of competing interest

The authors declare that they have no known competing financial interests or personal relationships that could have appeared to influence the work reported in this paper.

Acknowledgements

This work was supported by the National Natural Science Foundation of China (no. 21871192 and 81771114) and Sichuan Science and Technology Program (no. 2018JY0559). We acknowledge the comprehensive training platform of the specialized laboratory of the College of Chemistry, Sichuan University, for material analysis. We would like to thank the Analytical & Testing Center of Sichuan University for CCD X-ray single crystal diffractometer work and circular dichroism

spectrometer work. We are grateful to Daibing Luo and Yani Xie for help with the single crystal and circular dichroism measurements.

Appendix A. Supplementary data

Supplementary data to this article can be found online at https://doi.org/10.1016/j.dyepig.2020.108851.

References

[1] Valeur B. Molecular fluorescence: principles and applications. Wiley; 2002.
[2] Mitschke U, Bauerle P. The electroluminescence of organic materials. J Mater Chem 2000;10:1471–507.
[3] Xiang HF, Cheng JH, Ma XF, Zhou XG, Chruma J. Near-Infrared phosphorescence: materials and applications. J. Chem. Soc. Rev. 2013;42:6128–85.
[4] Li Y, Yao JW, Wang C, Zhou XH, Xu YW, Hanif M, Qiu X, Hu DH, Ma DG, Ma YG. Highly efficient deep-red/near-infrared D-A chromophores based on naphthothiadiazole for OLEDs applications. Dyes Pigments 2020;173:07960.
[5] Lan Y, Li G, Wang Z, He YH, Liu YC, He L. Fluorine-free blue-emitting cationic iridium complexes with oxadiazole-type cyclometalating ligands and their use in light- emitting electrochemical cells. Dyes Pigments 2017;144:158–67.
[6] Costa RD, Orti E, Bolink HJ. Recent advances in light-emitting electrochemical cells. Pure Appl Chem 2011;83:2115–28.
[7] Singh-Rachford TN, Castellano FN. Photon upconversion based on sensitized triplet–triplet annihilation. Coord Chem Rev 2010;254:2560–73.
[8] Zhao JZ, Ji S, Guo HM. Triplet–triplet annihilation based upconversion: from triplet sensitizers and triplet acceptors to upconversion quantum yields. RSC Adv 2011;1:937–50.
[9] Kim HN, Lee MH, Kim HJ, Kim JS, Yoon J. A new trend in rhodamine-based chemosensors: application of spirolactam ring-opening to sensing ions. Chem Soc Rev 2008;37:1465–72.
[10] Zhao Q, Li FY, Huang CH. Phosphorescent chemosensors based on heavy-metal complexes. Chem Soc Rev 2010;39:3007–30.
[11] Zhang JF, Zhou Y, Yoon J, Kim JS. Recent progress in fluorescent and colorimetric chemosensors for detection of precious metal ions (silver, gold and platinum ions). Chem Soc Rev 2011;40:3416–29.
[12] Zhao Q, Huang CH, Li FY. Phosphorescent heavy-metal complexes for bioimaging. Chem Soc Rev 2011;40:2508–24.
[13] Yin HY, Tang J, Zhang JL. Sulfur speciation defined subcellular localization of coumarin derivatives: correlation of structural relationship to biological behaviors. Chin Chem Lett 2018;29:267–70.
[14] Zhao JZ, Ji SM, Chen YH, Guo HM, Yang P. Excited state intramolecular proton transfer (ESIPT): from principal Photophysics to the development of new chromophores and applications in fluorescent molecular probes and luminescent materials. Phys Chem Chem Phys 2012;14:8803–17.
[15] Kwon JE, Park SY. Advanced organic optoelectronic materials: harnessing excited-state intramolecular proton transfer (ESIPT) process. Adv. Mater. 2011;23:3615–42.
[16] Luo J, Xie Z, Lam WY, Cheng L, Chen H, Qiu C, Kwok HS, Zhan X, Liu Y, Zhu D, Tang BZ. Aggregation-induced emission of 1-methyl-1,2,3,4,5-pentaphenylsilole. Chem. Commun 2001:1740–1.
[17] Hong Y, Lam JWY, Tang BZ. Aggregation-induced emission. Chem Soc Rev 2011;40:5361–88.
[18] Adburahman A, Wang L, Zhang ZX, Feng YT, Zhao YH, Zhang M. Novel triazole-based AIE materials: dual-functional, highly sensitive and selective fluorescence probe. Dyes Pigments 2020;174:108050.
[19] Markov P. Light-induced tautomerism of β-dicarbonyl compounds. Chem Soc Rev 1984;13:69–70.
[20] Dziembowska T, Rozwadowski Z. Application of the deuterium isotope effect on NMR chemical shift to study proton transfer equilibrium. Curr Org Chem 2001;5:289–313.
[21] Temprado M, Roux MV, Umnahanant P, Zhao H, Chickos JS. The thermochemistry of 2,4-pentanedione Revisited: observance of a nonzero enthalpy of mixing between tautomers and its effects on enthalpies of formation. J Phys Chem B 2005;109:12590–5.
[22] Zhang X, Li ZC, Xu N, Li KB, Lin S, Lu FZ, Du FS, Li FM. β-Diketones bearing electron-donating chromophores and a novel β-triketone: synthesis and reversible fluorescence behaior. Tetrahedron Lett 2006;47:2623–6.
[23] Liu X, Xu D, Lu R, Li B, Qian C, Xue P, Zhang X, Zhou H. Luminescent organic 1D nanomaterials based on bis(β-diketone)carbazole derivatives. Chem Eur J 2011;17:1660–9.
[24] Qian C, Liu M, Hong G, Xue P, Gong P, Lu R. Luminescent organogels based on triphenylamine functionalized β-diketones and their difluoroboron complexes. Org Biomol Chem 2015;13:2986–98.
[25] Kitagawa Y, Yachi R, Nakanishi T, Fushimi K, Hasegawa Y. J-type heteroexciton coupling effect on an asymmetric donor–acceptor–donor-type fluorophore. J Phys Chem A 2017;121:4613–8.
[26] Chou PT, Pu SC, Cheng YM, Yu WS, Yu YC, Hung FT, Hu WP. Femtosecond dynamics on excited-state proton/charge-transfer reaction in 4'-N,N-Diethylamino-3-hydroxyflavone. The role of dipolar vectors in constructing a rational mechanism. J Phys Chem A 2005;109:3777–87.
[27] Zamotaiev OM, Postupalenko VY, Shvadchak VV, Pivovarenko VG, Klymchenko AS, Mely Y. Improved hydration-sensitive dual-fluorescence labels for monitoring Peptide−Nucleic acid interactions. Bioconjugate Chem 2011;22:101–7.
[28] Tang KC, Chang MJ, Lin TY, Pan HA, Fang TC, Chen KY, Hung WY, Hsu YH, Chou PT. Fine tuning the energetics of excited-state intramolecular proton transfer (ESIPT): white light generation in A single ESIPT system. J Am Chem Soc 2011;133:17738–45.
[29] Cheng X, Wang K, Huang S, Zhang H, Zhang H, Wang Y. Organic crystals with near-infrared amplified spontaneous emissions based on 2'-hydroxychalcone derivatives: subtle structure modification but great property change. Angew Chem Int Ed 2015;54:8369–73.
[30] Tang B, Zhang H, Cheng X, Ye K, Zhang H. 1,3-Diaryl-β-diketone organic crystals with red amplified spontaneous emission. ChemPlusChem 2016;81:1320–5.
[31] Li J, Wu Y, Xu Z, Liao Q, Zhang H, Zhang Y, Xiao L, Yao J, Fu H. Tuning the organic microcrystal laser wavelength of ESIPT-active compounds via controlling the excited enol* and keto* emissions. J Mater Chem C 2017;5:12235–40.
[32] Priyadarsini KI. Photophysics, photochemistry and photobiology of curcumin: studies from orgnic solutions, bio-mimetics and living cells. J. Photoch. Photobio. C 2009;10:81–95.
[33] Patra D, Barakat C. Synchronous fluorescence spectroscopic study of solvatochromic curcumin dye. Spectrochim Acta 2011;79:1034–41.
[34] Li Y, Zeng L, Zhong C, Dong X, Mao Z, Liu Z, Lv S, Zhang Z. A two-photon dye with favorable photophysical properties and ultrahigh polarity sensitivity designed by utilizing the tautomerism of β-diketone. Adv. Optical Mater. 2017;5:1600696.
[35] Nagai A, Kokado K, Nagata Y, Arita M, Chujo Yoshiki. Highly intense fluorescent diarylboron diketonate. J Org Chem 2008;73:8605–7.
[36] Wang XF, Xiao H, Chen PZ, Zheng Yang Q, Chen B, Tung CH, Chen YZ, Wu Li Z. Pure organic room temperat ure phosphorescence from excited dimers in self-assembled nanoparticles under visible and near-infrared irradiation in water. J Am Chem Soc 2019;141:5045–50.
[37] Butler T, Morris WA, Samonina-Kosicka J, Fraser CL. Mechanochromic luminescence and aggregation induced emission of dinaphthoylmethane β-diketones and their boronated counterparts. ACS Appl Mater Interfaces 2016;8:1242–51.
[38] Wu XJ, Meng QH, Zhang Q, Fan LY, Xiao H, Cao CX. Glycoprotein flfluorescent speed sensing by newly-synthesized boronic complex probe and chip supramolecular electrophoresis. Sensor Actuator B Chem 2020;309:127773.
[39] Eliseeva SV, Bunzli JCG. Lanthanide luminescence for functional materials and bio-sciences. Chem Soc Rev 2010;39:189–227.
[40] Flamigni L, Barbieri A, Sabatini C, Ventura B, Barigelletti F. Photochemistry and Photophysics of coordination compounds: iridium. Top Curr Chem 2007;281:143–203.
[41] Li J, Djurovich PI, Alleyne BD, Yousufuddin M, Ho NN, Thomas JC, Peters JC, Bau R, Thompson ME. Synthetic control of excited-state properties in cyclometalated Ir(III) complexes using ancillary ligands. Inorg Chem 2005;44:1713–27.
[42] Wang C, Amiri M, Endean RT, Perez OM, Varley S, Rennie B, Rasu L, Bergens SH. Modular construction of photoanodes with covalently bonded ruand Ir-polypyridyl visible light chromophores sens. ACS Appl Mater Interfaces 2018;10:24533–42.
[43] Murphy L, Williams JAG. Luminescent platinum compounds: from molecules to OLEDs. Top Organomet Chem 2010;28:75–111.
[44] Sun Y, Yang X, Liu B, Dang J, Li Y, Zhou G, Wu Z, Wong WY. Aggregation-induced emission triggered by the radiative-transition-switch of a cyclometallated Pt(II) complex. J Mater Chem C 2019;7:12552–9.
[45] Pu L. Fluorescence of organic molecules in chiral recognition. Chem Rev 2004;104:1687–716.
[46] Pu L. Enantioselective fluorescent sensors: a tale of BINOL. Acc Chem Res 2012;45:150–63.
[47] Zhang X, Yin J, Yoon J. Recent advances in development of chiral fluorescent and colorimetric sensors. Chem Rev 2014;114:4918–59.
[48] Pu L. Simultaneous determination of concentration and enantiomeric composition in fluorescent sensing. Acc Chem Res 2017;50:1032–40.
[49] Xu XM, Qu L, Song JT, Wu DH, Zhou XG, Xiang HF. A simple and visual approach for enantioselective recognition through supramolecular gels with specific selectivity. Chem Commun 2019;55:9873–6.
[50] Sanchez-Carnerero EM, Agarrabeitia AR, Moreno F, Maroto BL, Muller G, Ortiz MJ, delaMoya S. Circularly polarized luminescence from simple organic molecules. Chem Eur J 2015;21:13488–500.
[51] Kumar J, Nakashima T, Kawai T. Circularly polarized luminescence in chiral molecules and supramolecular assemblies. J Phys Chem Lett 2015;6:3445–52.
[52] Song F, Xu Z, Zhang Q, Zhao Z, Zhang H, Zhao W, Qiu Z, Qi C, Zhang H, Sung HHY, Williams ID, Lam JWY, Zhao Z, Qin A, Ma D, Tang BZ. Highly efficient circularly polarized electroluminescence from aggregation-induced emission luminogens with amplified chirality and delayed fluorescence. Adv Funct Mater 2018;28:1800051.
[53] Song JT, Wang M, Xu XM, Qu L, Zhou XG, Xiang HF. 1D-helical platinum(ii) complexes bearing metal-induced chirality, aggregation-induced red phosphorescence, and circularly polarized luminescence. Dalton Trans 2019;48:4420–8.
[54] Wu ZG, Yan ZP, Luo XF, Yuan L, Liang WQ, Wang Y, Zheng YX, Zuo JL, Pan Y. Non-doped and doped circularly polarized organic light-emitting diodes with high performances based on chiral octahydro-binaphthyl delayed fluorescent luminophores. J Mater Chem C 2019;7:7045–52.
[55] Qu L, Xu XM, Song JT, Wu DH, Wang L, Zhou WL, Zhou XG, Xiang HF. Solid-state photochromic molecular switches based on axially chiral and helical spiropyrans. Dyes Pigments 2020;181:108597.

[56] Kim E, Felouat A, Zaborova E, Ribierre JC, Wu JW, Senatore S, Matthews C, Lenne PF, Baffffert C, Karapetyan A, Giorgi M, Jacquemin D, Ponce-Vargas M, Guennic BL, Fages F, D'Aléo A. Borondifluoride complexes of hemicurcuminoids as bio-inspired push–pull dyes for bioimaging. Org Biomol Chem 2016;14:1311–24.
[57] Wang YW, Liu SB, Ling WJ, Peng Y. A fluorescent probe for relay recognition of homocysteine and group IIIA ions including Ga(III). Chem Commun 2016;52:827–30.
[58] Bougauchi M, Watanabe S, Arai T, Sasai H, Shibasaki M. Catalytic asymmetric epoxidation of α,β-unsaturated Ketones promoted by lanthanoid complexes. J Am Chem Soc 1997;119:2329–30.
[59] Inagaki S, Saito K, Suto S, Aihara H, Sugawara A, Tamura S, Kawano T. Synthesis of 5-aryl-3(2H)-furanones using intramolecular cyclization of sulfonium salts. J Org Chem 2018;83:13834–46.
[60] Shen GY, Gou F, Cheng JH, Zhang XH, Zhou XG, Xiang HF. Chiral and non-conjugated fluorescent salen ligands: AIE, anion probes, chiral recognition of unprotected amino acids, and cell imaging applications. RSC Adv 2017;7:40640–9.
[61] Wang M, Cheng CQ, Song JT, Wang J, Zhou XG, Xiang HF, Liu J. Multiple hydrogen bonds promoted ESIPT and AIE-active chiral salicylaldehyde hydrazide. Chin J Chem 2018;36:698–707.
[62] Qu L, Li CB, Shen GY, Gou F, Song JT, Wang M, Xu XM, Zhou XG, Xiang HF. Syntheses, crystal structures, chirality and aggregation-induced phosphorescence of stacked binuclear Platinum(II) complexes with bridging salen ligands. Mater. Chem. Front. 2019;3:1199–208.
[63] Wang M, Cheng CQ, Li CB, Wu DH, Song JT, Wang J, Zhou XG, Xiang HF, Liu J. Smart, chiral, and nonconjugated cyclohexane-based bis-salicylaldehyde hydrazides: multi-stimuli-responsive, turn-on, ratiometric, and thermochromic fluorescence, single-crystal structures via DFT calculations. J Mater Chem C 2019;7:6767–78.
[64] Cheng JH, Wei KY, Ma XF, Zhou XG, Xiang HF. Synthesis and photophysical properties of colorful salen-type Schiff bases. J Phys Chem C 2013;117:16552–63.
[65] Cheng JH, Ma XF, Zhang YH, Liu JY, Zhou XG, Xiang HF. Optical chemosensors based on transmetalation of salen-based Schiff base complexes. Inorg Chem 2014;53:3210–9.
[66] Wang YJ, Pan MH, Cheng AL, Lin LI, Ho YS, Hsieh CY, Lin JK. Stability of curcumin in buffer solution and characterization of its degradetion products. J Pharmaceut Biomed Anal 1997;15:1867–76.
[67] Gross KC, Seybold PG. Substituent effects on the physical properties and pKa of phenol. Int J Quant Chem 2001;85:569–79.
[68] Tumambac GE, Francis CJ, Wolf C. Stability of 2-benzoylcyclohexanone: unexpected solvent effects on the rate of racemization. Chirality 2005;17:171–6.
[69] Godsi O, Turner B, Suwinska K, Peskin U, Eichen Y. Enol−Enamine tautomerism in crystals of 1,3-Bis(pyridin-2-yl) propan-2-one: A combined crystallographic and quantum-chemical investigation of the effect of packing on tautomerization processes. J Am Chem Soc 2004;126:13519–25.
[70] Bertolasi V, Ferretti V, Gilli P, Yao X, Li CJ. Substituent effects on keto–enol tautomerization of β-diketones from X-ray structural data and DFT calculations. New J Chem 2008;32:694–704.
[71] Iglesias E. Tautomerization of 2-acetylcyclohexanone. 1. Characterization of Keto−Enol/enolate equilibria and reaction rates in water. J Org Chem 2003;68:2680–8.
[72] Sloop JC, Bumgardner CL, Washington G, Loehle WD, Sankar SS, Lewis AB. Keto-enol and enol tautomerism in trifluoromethyl-β-diketones. J Fluor Chem 2006;127:780–6.
[73] Parimita SP, Ramshankar YV, Suresh S, Guru Row TN. Redetermination of curcumin: (1E,4Z,6E)-5-hydroxy-1,7-bis (4-hydr–oxy-3-meth-oxy-phen-yl)hepta-1,4,6-trien-3-one. Acta Crystallogr E 2007;63. o860−o872.
[74] Cheng JH, Zhang YH, Ma XF, Zhou XG, Xiang HF. Colorimetric and fluorescent pH and Cu^{2+} probes induced by photoisomerization of a maleonitrile-based salen ligand. Chem Commun 2013;49:11791–3.
[75] Cheng JH, Gou F, Zhang XH, Shen GY, Zhou XG, Xiang HF. A class of multiresponsive colorimetric and fluorescent pH probes via three different reaction mechanisms of salen complexes: a selective and accurate pH measurement. Inorg Chem 2016;55:9221–9.
[76] Zhang XH, Shi J, Shen GY, Gou F, Cheng JH, Zhou XG, Xiang HF. Non-conjugated fluorescent molecular cages of salicylaldehyde-based tri-schiff bases: AIE, enantiomers, mechanochromism, anion hosts/probes, and cell imaging properties. Mater. Chem. Front. 2017;1:1041–50.
[77] H Zhang X, Shi J, Song JT, Wang M, Xu XM, Qu L, Zhou XG, Xiang HF. Nonconjugated fluorescent molecular cages of trinuclear fluoroborate complexes with salicylaldehyde-based Schiff base ligands. ACS Omega 2018;23:8992–9002.
[78] Zhou Y, Zhang D, Zhang Y, Tang Y, Zhu D. Tuning the CD spectrum and optical rotation value of a new binaphthalene molecule with two spiropyran Units: mimicking the function of a molecular "AND" logic gate and a new chiral molecular switch. J Org Chem 2005;70:6164–70.
[79] Chaolumen H, Ito logo, Itami K. An axially chiral 1,1′-biazulene and its π-extended derivative: synthesis, structures and properties. Chem Commun 2019;55:9606–9.

Dehua Wu is a graduate student at College of Chemistry, Sichuan University, Chengdu, China. Her fields of interests include organic optical materials and sensors.

Xinyi Fang is a graduate student at State Key Laboratory of Oral Diseases, Department of Orthodontics, West China Hospital of Stomatology, Sichuan University, Chengdu, China. Her fields of interests include cell biology and oral diseases.

Jintong Song is a graduate student at College of Chemistry, Sichuan University, Chengdu, China. His fields of interests include organic optical materials and sensors.

Lang Qu is a graduate student at College of Chemistry, Sichuan University, Chengdu, China. His fields of interests include organic optical materials and sensors.

Xiangge Zhou is a professor at College of Chemistry, Sichuan University, Chengdu, China. His research interests include the synthesis and catalysis of organometallic compounds and asymmetric synthesis.

Haifeng Xiang is a professor at College of Chemistry, Sichuan University, Chengdu, China. His research interests include fluorescent/phosphorescent sensor and organic optoelectronic materials.

Jun Wang is a professor at College of State Key Laboratory of Oral Diseases, Department of Orthodontics, West China Hospital of Stomatology, Sichuan University, Chengdu, China. His research interests include cell biology and oral diseases.

Jin Liu is a professor at Laboratory of Stem Cell Biology, State Key Laboratory of Biotherapy, West China Hospital, Sichuan University, Chengdu, China. Her research interests include cell biology and biotherapy